MATERIALS SCIENCE

Lifting a sessile oil drop from a superamphiphobic surface with an impacting one

Olinka Ramírez-Soto[1,2,3]*, Vatsal Sanjay[2]*, Detlef Lohse[2,3], Jonathan T. Pham[4†], Doris Vollmer[1†]

Copyright © 2020 The Authors, some rights reserved; exclusive licensee American Association for the Advancement of Science. No claim to original U.S. Government Works. Distributed under a Creative Commons Attribution NonCommercial License 4.0 (CC BY-NC).

Colliding drops are encountered in everyday technologies and natural processes, from combustion engines and commodity sprays to raindrops and cloud formation. The outcome of a collision depends on many factors, including the impact velocity and the degree of alignment, and intrinsic properties like surface tension. Yet, little is known on binary impact dynamics of low-surface-tension drops on a low-wetting surface. We investigate the dynamics of an oil drop impacting an identical sessile drop sitting on a superamphiphobic surface. We observe five rebound scenarios, four of which do not involve coalescence. We describe two previously unexplored cases for sessile drop liftoff, resulting from drop-on-drop impact. Numerical simulations quantitatively reproduce the rebound scenarios and enable quantification of velocity profiles, energy transfer, and viscous dissipation. Our results illustrate how varying the offset from head-on alignment and the impact velocity results in controllable rebound dynamics for oil drop collisions on superamphiphobic surfaces.

Downloaded from http://advances.sciencemag.org/ on September 7, 2020

INTRODUCTION

When a liquid drop impacts a sessile one of an identical liquid, it is intuitively expected that both drops coalesce. This process is commonly observed in day-to-day examples, such as rain or drops from a leaky faucet. However, coalescence can be obstructed by a thin layer of air between the two drops (*1*–*3*). Insufficient thinning of this air layer during impact even enables water drops to bounce from perfectly hydrophilic surfaces, which they would otherwise wet (*4*–*6*). In the late 1800s, Reynolds (*7*) noticed that water drops can glide over a pool because of this air layer. A vapor layer also governs the Leidenfrost effect (*8*–*10*), where a drop hovers over a superheated surface. As a result, drop bouncing, coalescence, and spreading can all be observed depending on the intrinsic properties of the liquid, as well as external parameters, such as the background pressure, the collision velocity, and the impact parameter describing whether the collision is head-on or off-centered (*11*–*24*). Despite progress in the experimental characterization of the impact dynamics, quantitative modeling of the velocity fields and energy transfer is lacking.

In various situations, drops can impact a sessile drop. The impact dynamics of a water drop on a sessile water drop has been characterized for surfaces of varying wettability (*19*, *21*, *25*–*27*). On superhydrophobic surfaces, a water drop impacting another one can lead to drop removal after coalescence. Sufficient transfer of kinetic energy from the impact event turns the two drops into a single merged drop and leads to bouncing after coalescence (*14*, *28*–*31*). Alternatively, both drops can also rebound from the surface if sufficient energy is exchanged during impact (*21*, *32*). However, drops are not always water. Impact of low interfacial tension drops can be encountered in chemical shielding, additive manufacturing, and aerosol collection of low-surface-tension liquids (*33*–*35*). In agriculture, it is essential to ensure that pesticides and other chemicals sprayed on wet leaves do not roll off and contaminate the surroundings (*36*), which can contain surfactants that lower the interfacial tension. Moreover, splashing and impact of oil drops are also commonly observed in kitchen pans and countertops.

While studies of binary water drop impact on superhydrophobic surfaces exist, investigation of low-interfacial-tension drop-on-drop impact on superamphiphobic surfaces has been hampered by the limited number of techniques to design nonwetting surfaces. Advanced techniques in fabricating high-end oil-repellent surfaces, including spray coating and three-dimensional printing, are continuing to be developed (*37*–*39*). This enables studies of drop impact on nonwetting surfaces of low-surface-tension liquids (*40*). From both a fundamental perspective as well as to access the properties of these surfaces, understanding of binary drop impact of low-surface-tension liquids is valuable. What scenarios exist for drop-on-drop impact of oil on a superamphiphobic surface? How is energy transferred between the drops? Intuitively, the rebound of oil drops from a surface by impact with another oil drop seems more difficult than water for the following reasons. (i) The surface tension, γ, of most hydrocarbon oils (25 mN/m) is much lower than that of water (72 mN/m). Smaller γ reduces the transfer of surface energy to kinetic energy during the coalescence. This implies that the drops have less energy to rebound. (ii) Sessile oil drops typically have a large contact size. On a flat surface, the receding contact angle is typically below 60° and often close to zero (*41*). Consequently, receding oil drops easily rupture before coming off the surface. (iii) On a superamphiphobic surface, oil drops display large apparent contact angles (*37*, *42*). However, the true liquid-solid contact angle is still small, leaving oil drops in a metastable state; that is, they can creep into the surface (*43*). Moreover, pressure as low as a few hundred Pascal is sufficient to transition the drop from the metastable Cassie state to wet the surface thoroughly (*42*, *44*). The height of the energy barrier—related to the so-termed impalement pressure—depends on details of the coating and the liquid under investigation (*43*). (iv) The low surface tension of oil means that the drop is easily deformable, which may give rise to enhanced viscous dissipation and energy loss upon impact. The drop can also locally impale the surface during impact (*45*, *46*).

[1]Max Planck Institute for Polymer Research, Mainz, Germany. [2]Physics of Fluids Group, Max Planck Center for Complex Fluid Dynamics, Mesa+ Institute, and J.M. Burgers Center for Fluid Dynamics, University of Twente, Enschede, Netherlands. [3]Max Planck Institute for Dynamics and Self-Organization, 37077 Göttingen, Germany. [4]Department of Chemical and Materials Engineering, University of Kentucky, Lexington, KY 40506, USA.
*These authors contributed equally to this work
†Corresponding author. Email: vollmerd@mpip-mainz.mpg.de (D.V.); jonathan.pham@uky.edu (J.T.P.)

In this contribution, we experimentally and numerically investigate the dynamics of a low-surface-tension oil drop impacting a sessile drop of the same liquid, resting on a superamphiphobic surface (Fig. 1A). We find that the impacting oil drop can lift the resting drop off the surface without ever coalescing. We find four rebound scenarios without coalescence: (i) both drops rebound, (ii) two scenarios where the impacting drop rebounds while the sessile drop remains, and (iii) the sessile drop rebounds while the impacting drop remains on the surface. We illustrate how these impact outcomes are governed by the Weber number and the extent of offset from a head-on collision. Direct numerical simulations (DNS) provide a quantitative description of (i) the velocity of both drops and of the surrounding medium, (ii) how energy is transferred between the two drops during impact, and (iii) the viscous dissipation during impact and rebound. This methodology allows for a quantitative comparison of experimental and numerical data of the rebound dynamics.

RESULTS

Approach

In our experiments, a sessile oil drop is gently positioned on a superamphiphobic surface and then impacted with a second identical oil drop (Fig. 1A). The superamphiphobic surface is composed of a ~20-μm-thick layer of templated candle soot (*10*, *47*). Candle soot consists of a porous network of 50± 20–nm–sized carbon nanobeads. Making use of chemical vapor deposition of tetraethyl orthosilicate catalyzed by ammonia, a ~25-nm-thick layer of silica is deposited over the porous nanostructures to increase the mechanical stability of the fragile network (Fig. 1A-i and fig. S1). The soot-templated silica network is fluorinated with trichloroperfluoroctylsilane to lower the surface energy, producing a superamphiphobic surface that repels water and most oils. As a model oil, we use hexadecane for its low surface tension, low volatility, homogeneous properties, and Newtonian behavior. A drop of hexadecane (Fig. 1A-ii) exhibits an apparent contact angle of $\Theta^{app} = 164° \pm 1°$, an apparent receding contact angle of $\Theta_r^{app} = 158° \pm 3°$, and an apparent advancing contact angle of $\Theta_a^{app} \approx 180°$ (*48*), as determined by confocal microscopy (Fig. 1A-iii and figs. S2 and S3). Low lateral adhesion of hexadecane is confirmed by measuring a low roll-off angle of $\alpha = 3° \pm 2°$ (*49*).

For our drop impact studies, a sessile drop of hexadecane is gently placed on this superamphiphobic surface with a needle connected to a syringe pump (dosing rate, 2 ml/hour). When gravity exceeds the drop-needle adhesion, the drop releases from the needle; this results in a drop volume of $V \approx 3$ μl (Fig. 1A). This volume corresponds to a Bond number of 0.3 ($Bo = \rho_l g R^2/\gamma$, where ρ_l is the density of the liquid, g is the gravitational acceleration, and R is the radius of a spherical droplet of identical volume). The Bond number relates gravitational forces to surface forces, reflecting how gravity affects the shape of the sessile drop. Note that a low Bond number implies that a spherical cap can describe the drop. However, it does not provide insight on whether the drop passes the Cassie-to-Wenzel transition. Still, the shape of the drop is important as it forms the initial

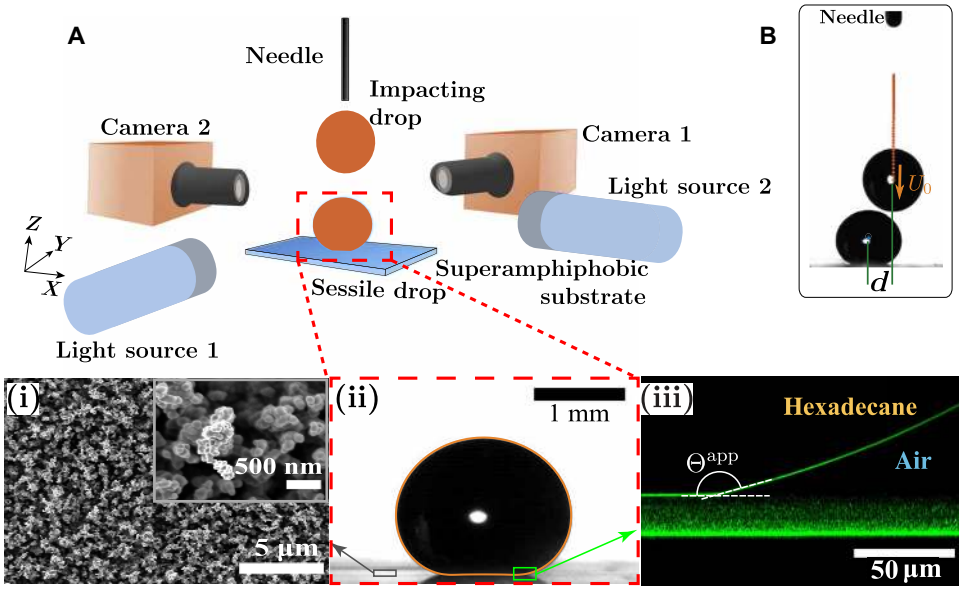

Fig. 1. Experimental approach and the sessile drop. (**A**) Sketch of the experimental setup for binary drop impact on superamphiphobic surfaces. The needle is fixed to set the impacting height in the *Z* direction and the relative distance between the sessile and impacting drops. The sessile drop is first centered along the *YZ* plane. Then, the impacting drop is dispensed from the needle while the impact is monitored with camera 2. Camera 1 is used to determine the relative positions of the drops in the *X* direction. The cameras and the light sources are aligned to observe the impact both in the *XZ* and *YZ* planes. Insets: (i) SEM image of a soot-templated surface at two magnifications. (ii) Hexadecane drop ($V \approx 3$ μl) resting on the superamphiphobic surface. The orange contour is the solution of Eq. 1 for a corresponding Bond number $Bo = 0.3$. (iii) Confocal image showing a drop of hexadecane on the superamphiphobic surface. The image illustrates the apparent contact angle of the drop with the surface ($\Theta_{app} \approx 164°$). The image is taken in reflection mode, i.e., no dye was added to the hexadecane. Reflection of light results from the differences between the refractive indices of hexadecane (1.43), air (1.0), and glass and silica (~1.46). The superamphiphobic layer consists mostly of air, and thus, its refractive index is close to 1. Therefore, the horizontal glass-superamphiphobic layer and the hexadecane-superamphiphobic layer interfaces are visible. The superamphiphobic layer itself is visible as a diffuse pattern, resulting from the reflection of light from the silica nanoparticles. (**B**) Image showing an off-center collision. The impact parameter is $\chi = d/(2R)$. Photo credit: Olinka Ramírez-Soto, Max Planck Institute for Polymer Research.

Downloaded from http://advances.sciencemag.org/ on September 7, 2020

condition for the numerical simulation. To calculate and confirm this shape numerically, we solved the Young-Laplace equation

$$-\frac{\partial P'}{\partial X_i} + (\kappa - \Delta\rho BoZ)\,\delta_s\, n_i = 0 \qquad (1)$$

In Eq. 1, P' refers to the reduced pressure [as defined in (*50*)], X_i refers to the coordinate system unit vector, $Bo\,Z$ is the gravitational potential, κ is the curvature of the liquid-gas interface, $\Delta\rho$ is the normalized density difference across this interface (nondimensionalized with ρ_l), δ_s is the Kronecker delta function (1 at the interface and 0 otherwise), and n_i is the unit vector normal to the interface. Note that all equations in this manuscript are written using the Cartesian tensor notation. The shape of the drop is calculated by solving Eq. 1 and matches well with the experiments (Fig. 1A-ii).

The control parameters of the drop collision, determining the outcome, are the Weber number (We), which is related to the impact velocity (U_0), and the impact parameter (χ), which describes the offset from head-on alignment of the two colliding drops. The impact velocity, U_0, is controlled by positioning the needle to a defined height (Fig. 1A). The corresponding Weber number, $We = \rho_l U_0^2 R^2/\gamma$, compares fluid inertia and surface tension, where $\rho_l = 770$ kg/m^3 is the density of the hexadecane and $\gamma = 27.5$ mN/m is the surface tension. In our experiments, the Weber number ranges from 0.02 to 9. The substrate is then translated laterally to position the drop in the X and Y directions. At an identical dosing rate, a second drop is released with an identical volume, $V \approx 3$ μl, and impacts the sessile drop. Two high-speed cameras are perpendicularly positioned to capture the dynamics of the drops in the X, Y, and Z directions. The impact parameter of the two drops is given by the ratio [$\chi = d/(2R)$], where d is the horizontal difference of the center of masses of the impacting drop and the sessile drop (Fig. 1B). Although we cannot exactly predict the impact parameter beforehand, the two-camera system allows us to precisely measure the offset from head-on alignment by image analysis. $\chi = 0$ describes a perfect head-on collision, whereas $\chi = 1$ corresponds to the situation when the two drops merely brush each other ($d = 2R$).

Experimental observations

When varying the offset from head-on alignment χ and the Weber number We, six outcomes for the impact dynamics are observed, termed cases I to VI (Fig. 2). The column A images are taken just as the collision starts ($t = 0$ ms) and are used to quantify the impact parameter χ. Column B is at the point of maximum sessile drop compression, and column C demonstrates the shape of both drop just before they separate or coalesce. Column D illustrates the overall outcome of the collision event. We first consider the outcomes at $We \approx 1.5$ while varying χ. For a near-zero χ, case I is observed, which is a head-on collision (Fig. 2, movies S1 to S3, and fig. S4). During impact, both drops deform and spread radially and, as a result, show axial compression. The kinetic energy of the system is transferred to the surface energies of both deformed drops. Moving forward in time, both drops start to retract. The sessile drop transfers energy back to the impacting drop in the form of kinetic energy. Upon completion of the collision, the impacting drop bounces off while the sessile drop stays on the substrate. The sessile drop oscillates, hinting that it retains a part of the energy gained during impact. For a slightly higher offset, $\chi \lesssim 0.15$, case II is observed (movies S4 to S6 and fig. S5). The initial collision is similar to case I in that the drops collide, followed by vertical compression and lateral spreading. However,

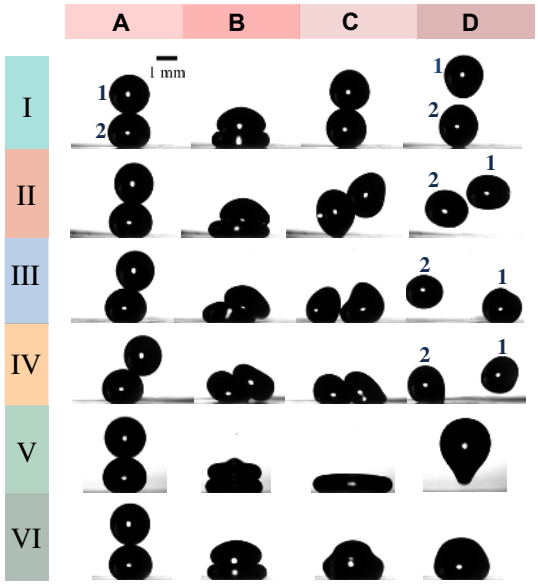

Fig. 2. Snapshots of the impact dynamics. Note that the drop labels 1 and 2 are for the impacting and sessile drop, respectively. Six outcomes (cases I to VI) are observed when varying the impact parameter χ and the Weber number (We). The rows correspond to different impact parameter for I to IV. The columns show characteristic stages of the collision process. A, just at collision; B, sessile drop at maximum compression; C, droplet shape just before separation or coalescence; D, final outcome of the impact. The height of the center of mass of the impacting, sessile, or coalesced drops is maximal. Volume of both drops is 3 μl. Case I: $We = 1.30$ and $\chi = 0.01$, the time stamps for each frame are $t_A = 0$ ms, $t_B = 8$ ms, $t_C = 20$ ms, and $t_D = 25$ ms. Case II: $We = 1.53$, $\chi = 0.08$; $t_A = 0$ ms, $t_B = 8$ ms, $t_C = 20$ ms, and $t_D = 24$ ms. Case III: $We = 1.44$, $\chi = 0.24$; $t_A = 0$ ms, $t_B = 8$ ms, $t_C = 20$ ms, and $t_D = 24$ ms. Case IV: $We = 1.48$, $\chi = 0.52$; $t_A = 0$ ms, $t_B = 5.5$ ms, $t_C = 7$ ms, and $t_D = 21$ ms. Case V: $We = 5.84$, $\chi = 0.08$; $t_A = 0$ ms, $t_B = 3.75$ ms, $t_C = 8.5$ ms, and $t_D = 25.5$ ms. Case VI: $We = 1.43$, $\chi = 0.03$; $t_A = 0$ ms, $t_B = 7.5$ ms, $t_C = 9$ ms, and $t_D = 17$ ms. Photo credit: Olinka Ramírez-Soto, Max Planck Institute for Polymer Research.

unlike case I, the deformations are no longer symmetric, and the sessile drop also lifts off the surface. The displacement for either drop with respect to the center of mass of the initial sessile drop is in opposing lateral directions. Further increasing of the offset from head-on alignment to $\chi \lesssim 0.5$, the impacting drop glides over the sessile drop and rolls on the substrate, as illustrated by case III (Fig. 2, $\chi = 0.24$; movies S7 to S9; and fig. S6). Unlike cases I and II, no rebound of the impacting drop is observed. Instead, the sessile drop lifts off the surface. As the impact parameter is increased even further ($\chi > 0.5$, case IV), the impacting drop still rolls over the sessile drop (movies S10 to S12 and fig. S7). However, during retraction, the impacting drop rebounds from the surface while the sessile drop moves along the surface.

In the above cases I to IV, the Weber numbers were kept constant at $We \sim 1.5$, while the offset was varied. However, the outcome of the impact event also varies with the Weber number. To provide a better intuition on how both χ and We affect the observed outcomes, we plot our data as a phase diagram (Fig. 3). When the Weber number is increased above $We \geq 6$, regardless of the impact parameter χ, we find coalescence of the two drops, as illustrated in case V (Fig. 2, movie S13, and fig. S8). In this regime, the air layer between the drops is unstable, which results in direct contact and subsequent coalescence. The coalesced drop reaches a maximum spreading

Downloaded from http://advances.sciencemag.org/ on September 7, 2020

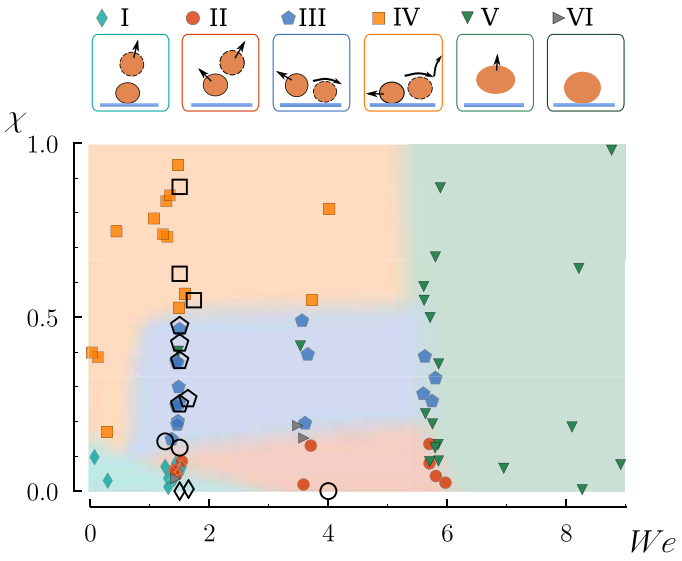

Fig. 3. Regime map. Phase diagram illustrating the observed cases as a function of the impact parameter, $\chi = d/(2R)$, and Weber number, *We*. The top sketches with the respective roman case number are the possible outcomes after the hexadecane drop impacted on the sessile hexadecane drop. In the image strip, the sessile drop is represented with the solid outline, and the impacting drop is represented with the dotted outline. The arrows represent the direction of motion after impact for each drop. In case III, the impacting drop has a horizontal curved arrow that represents the rolling of the drop over the sessile drop. In case IV, the impacting drop has two associated arrows. The horizontal curved arrow represents rolling over the sessile drop, and the vertical arrow denotes bouncing after the impact event. Each possible outcome is marked by a color and symbol for identification and corresponds to the sketched cases I to VI. Closed symbols correspond to experiments and open ones to numerical simulations. The transition zones between the different scenario regions are not sharp. The colors assigned to the different cases are meant as a guide to the eye.

diameter during impact (column C in Fig. 2). During retraction, the drop elongates vertically and ultimately detaches from the surface. Occasionally, drops coalesce without subsequent bouncing (case VI, movie S14 and fig. S9). Although this outcome is rarely observed and likely caused by surface defects, we present this result for the sake of completeness to demonstrate all observed outcomes. Moreover, to consider the generality of the scenarios presented for oil-on-oil drop impact, we also tested water-on-water drop impact. Similar scenarios are observed, as illustrated in fig. S10.

Direct numerical simulations

Although the experimental observations consistently illustrate how *We* and χ dictate the observed impact outcomes, they lack detailed information on the velocity fields and on how energy is transferred between both drops. To ascertain this information, we ran DNS and compared these results with our experimental data. For simulating noncoalescing droplets, we use geometric volume of fluid (VoF) (*51*) method with two distinct VoF tracers (see the Simulation methodology section for detailed discussions and implementation). This formulation ensures that drops cannot coalesce, reflecting the experimental situation where a finite air layer between the drops is preserved throughout the process.

We first ran four simulations choosing *We* and χ values within the regimes for cases I to IV, as denoted by open symbols in Fig. 3. The results are displayed in Fig. 4. The normalized times ($t^* = t/t_\gamma$, where t_γ is the inertial capillary time scale, $\sqrt{(\rho R^3)/\gamma}$) correspond to the stages of the process, as described by columns A to D in Fig. 2. As is evident from the top rows (orange drops), the simulations reproduce the general collision outcomes consistent with the snapshots of the impact dynamics (Fig. 2). Moreover, the DNS allow for quantifying the velocity vector fields for each of the cases (Fig. 4, bottom rows). These vector fields, combined with a calculation of the energy budget, render it possible to quantitatively explore the dynamics of the oil drop-on-drop collision process. To account for the kinetic energy (E_k), gravitational potential energy (E_p), surface energy (E_s), and dissipative losses (E_d), we numerically calculated the total energy of the system as

$$E = E_m + E_s + E_d \tag{2}$$

In Eq. 2, the total mechanical energy $E_m = E_k + E_p$, the surface energy E_s, and the energy dissipation E_d are calculated using a method similar to the one developed by Wildeman *et al.* (*52*). E_k includes the kinetic energy of the center of mass as well as the oscillation and rotational energies obtained in the reference frame that is translating with the center of mass of the individual drops. The details of these calculations are provided in Materials and Methods.

While keeping the Weber number at $We \sim O(1)$, the cases appear in order from I to IV with increasing offset position from head-on alignment χ. For all cases, the energy is initially contained in the mechanical energy of the impacting drop (i.e., its kinetic and potential energy) and the surface energy of the sessile drop. To describe the system energy of the DNS results presented in Fig. 4, we plot the full energy balances for each case in Fig. 5. For comparison convenience, the energies in Fig. 5 are normalized with this initial energy of the system.

Let us consider first a head-on collision where $\chi = 0$ (Figs. 4A and 5A and movies S2 and S3, case I), which is defined by a symmetric configuration. First, the momentum is transferred from the impacting drop to the sessile drop, as the sessile drop deforms. This transfer results in deceleration of the impacting drop. Moreover, the kinetic energy of the impacting drop transforms into the surface energy of the system. This transfer continues until $t^* = 1.84$ (Fig. 4A: column B) when the deformation in the two drops is maximum. Even at the moment of maximal elongation of both drops, the kinetic energy remains finite because of rotational flow within the drops (Fig. 4A, column B, velocity field) (*52*). The mechanical energy passes a minimum ($t^* = 1.84$) when the surface energy is maximal. For $t^* > 1.84$, the surface energy of the two drops is converted back into kinetic energy. Retraction of the sessile drop is hindered by the impacting one (Fig. 4A, column C), directly sitting on top of it. As a result, the sessile drop cannot lift off from the substrate, but it releases any extra energy by oscillations (movies S1 and S2). During impact, the drops lose approximately 20% of their initial energy through viscous dissipation inside the drops and the thin air layer between them (Fig. 5A). This dissipation occurs mainly during the initial stages of the process ($t^* < 3$). It should be noted that the surface tension (γ), viscosity (μ), and impact velocity (U_0) all affect viscous dissipation (*46*). These properties are related to the Ohnesorge number ($Oh = \mu/\sqrt{\rho\gamma R} \approx 0.03$), which compares viscous forces to inertia and surface tension forces, and the Weber number, $We = \rho U_0^2 R/\gamma \sim \mathcal{O}(1)$ [see Eq. 16 and (*53*)]. The dissipation observed in our case is lower than that reported previously for a single drop impact at comparable *Oh* and *We* on superhydrophobic (*52*) and superamphiphobic

Downloaded from http://advances.sciencemag.org/ on September 7, 2020

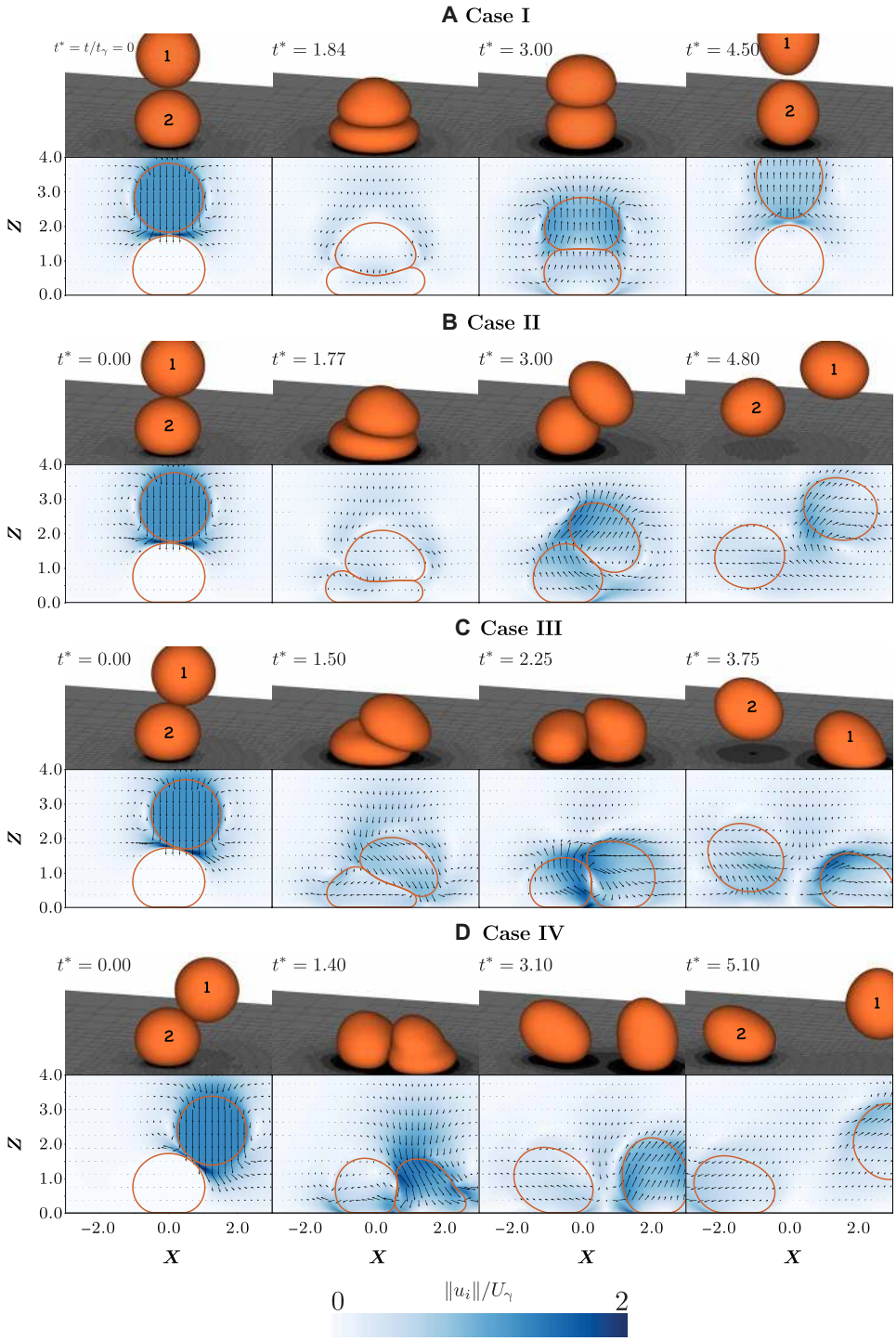

Fig. 4. Snapshots of DNS. Illustration of different phases of drop-on-drop collisions and the subsequent outcomes. (**A**) Case I: ($\chi = 0$) impacting drop bounces back and the sessile drops stays on the substrate; (**B**) case II: ($\chi = 0.08$) impacting drop bounces back and the sessile drop lifts off from the substrate; (**C**) case III: ($\chi = 0.25$) impacting drop stays on the substrate and the sessile drop lifts off; and (**D**) case IV: ($\chi = 0.625$) impacting drop bounces back and sessile drop stays on the substrate. For all these cases, $We = 1.5$. The drop labels 1 and 2 are for the impacting and sessile drops, respectively. t^* is the nondimensionalized time used for the numerical simulations and is given by $t = t/t_\gamma$, where t_γ is the inertial capillary time scale, $\sqrt{(\rho R^3)/\gamma}$. The absolute values of the normalized velocities vary between zero (white) and twice the inertial capillary velocity, $U_\gamma = \sqrt{\gamma/(\rho R)}$ (dark blue).

Downloaded from http://advances.sciencemag.org/ on September 7, 2020

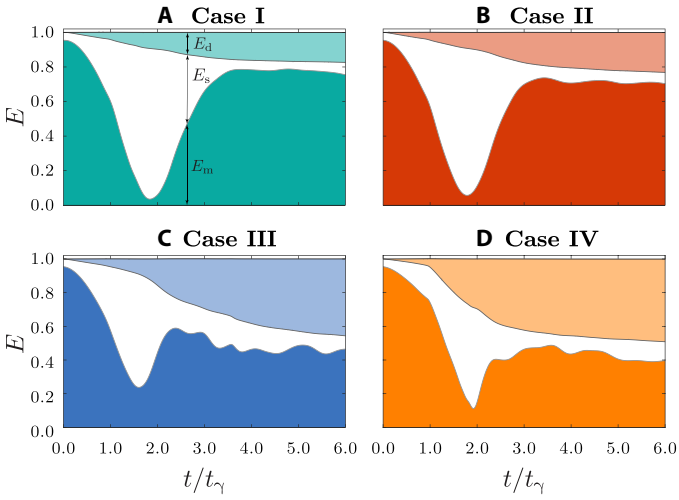

Fig. 5. Energy budget. The temporal variation of energy transfer elucidates different stages of the drop-on-drop impact process at *We* ~1. Initially, all the energy is stored as the mechanical energy of the impacting drop and surface energy of the sessile drop. Then, the mechanical energy of the system decreases and is transferred into the surface energy of the drops. This transfer is followed by a recovery stage where surface energy is transferred back into the mechanical energy of the system. A part of the energy is lost as viscous dissipation. This viscous dissipation takes into account the combined energy dissipated both in the liquid drops and the surrounding air. This calculation includes the air layers between the drops and between the drops and the superamphiphobic substrate. During impact, the drops (**A**) case I: $\chi = 0$, (**B**) case II: $\chi = 0.08$, (**C**) case III: $\chi = 0.25$, and (**D**) case IV: $\chi = 0.625$. E_m is the total mechanical energy of the system ($E_m = E_k + E_p$), E_s is the surface energy of the two drops, and E_d is the viscous dissipation in the system. Note that the total mechanical energy (E_m) includes the energy of center of mass of the drops ($E_m^{CM} = E_k^{CM} + E_p$) as well as the oscillation and rotational energies obtained in the reference frame that is translating with the center of mass of the individual drops.

substrates (*46*). In the case of a single drop impact, the velocity of the drop goes to zero quickly as it approaches a rigid substrate (*54*), leading to high dissipation close to the substrate (in the thin air layer and near the contact line). In the case of drop-on-drop impact, the sessile drop is deformable, decreasing the deceleration experienced by the impacting drop. As a result, the system retains almost 80% of its initial energy in the form of mechanical and surface energy of the drops.

For slightly off-center collisions where $\chi = 0.08$ (Figs. 4B and 5B and movies S5 and S6, case II), the initial collision is similar to case I; the drops collide, followed by vertical compression and lateral spreading. However, unlike case I, the impacting and the sessile drops lift off from the substrate. This feature results from the loss of axial symmetry of the velocity field for $\chi > 0$. During retraction, transfer of momentum from the compressed sessile drop back to the impacting drop occurs mainly along a vector pointing normal to the apparent contact zone. Moreover, the sessile drop attempts to regain its spherical shape (minimum surface energy state). As a result, the velocity field of the sessile drop is almost parallel to the contact zone, i.e., pointing to the upper left. These opposing orientations of the velocity fields cause the impacting drop to bounce off the sessile drop and the sessile drop to lift off from the substrate (see the velocity vector fields in Fig. 4B and movie S6). Viscous dissipation increases compared with a head-on-collision but still is maximum during the initial stages of the process ($t^* < 3.5$; Fig. 5B).

As the offset is further increased to $\chi = 0.25$ (Figs. 4C and 5C and movies S8 and S9, case III), the impacting drop glides over the sessile drop (facilitated by the thin air layer), and sufficient energy is transferred to lift the sessile drop from the substrate. This can be understood from the interplay of the velocity field and the contact time (Fig. 4C and movie S9). The relatively large offset from head-on alignment causes the averaged velocity field of the restoring impacting drop to point both almost parallel to the surface and downward, while the velocity field of the sessile drop is pointing upward. The large deformations of both drops are reflected in the evolution of the surface energy (Fig. 5C). The large deformations of both drops also cause an increase in viscous dissipation (E_d); at the end of the process, almost 50% of the initial energy is lost. Moreover, unlike cases I and II, viscous dissipation occurs not only in the drops but also in the thin air layer as the impacting drop approaches the substrate (*4*).

Last, if the offset from head-on alignment is increased even more to $\chi = 0.625$ (Figs. 4D and 5D and movies S11 and S12, case IV), the time of contact is insufficient to transfer enough energy to the sessile drop for liftoff (*55*). Moreover, the vector normal to the drop-drop contact area is farthest from vertical as compared with the normal vectors in other cases. That is, it points nearly horizontal. As a result, the sessile drop rolls along the substrate and the impacting drop instead rebounds from the surface, resembling typical drop-surface impact. In this case, most of the energy is retained by the impacting drop, as illustrated in Fig. 5D. Similar to case III, viscous dissipation accounts for almost 50% of the initial total energy. Although in cases I and IV the impacting drop rebounds while the sessile drop remains on the surface, we discriminate between both cases. For case I, the vector fields are symmetric around the $X = Y = 0$ axis, whereas for case IV, the vector fields are highly asymmetric, and the sessile drop rolls along the surface. Furthermore, in case IV, the impacting drop bounces off the substrate, as opposed to the sessile drop in case I.

These results indicate that the DNS provide a quantitative description of the impact dynamics. At this point, we investigate whether there is a one-to-one match of the experimental data and numerical simulations; this is done by comparing the drop boundaries and experimentally determined mechanical energies with the numerical predictions. Because we cannot exactly predict the impact parameter experimentally beforehand, we adjust the numerical simulations to the experimental data. We achieve a nearly quantitative agreement of the drop boundaries and experimental mechanical energies (Fig. 6). The different snapshots in Fig. 6 (i to iv) refer to the following time steps: (i) just at collision, (ii) sessile drop at maximum compression, (iii) droplet shape just before separation, and (iv) final outcome of the impact. We expect that slight deviations between the experimental and numerically determined drop boundaries result from marginal inaccuracies in the experimental determination of the offset parameter. However, the agreement is remarkably good, keeping in mind that there are no fitting parameters.

In Fig. 6 (A-v and B-v), we compare the measured experimental mechanical energies (data points) with those calculated using simulations (dotted lines). The calculated mechanical energies exceed the experimentally determined energies. To understand the origin of this discrepancy, one needs to consider that experimentally we are only able to measure the vertical and horizontal displacements to approximate the mechanical energy of each drop. The image analysis does not offer an easy route to quantify the contribution of the rotational and oscillation energies that are included in the numerically calculated mechanical energy, E_m. Therefore, to test whether neglecting

Downloaded from http://advances.sciencemag.org/ on September 7, 2020

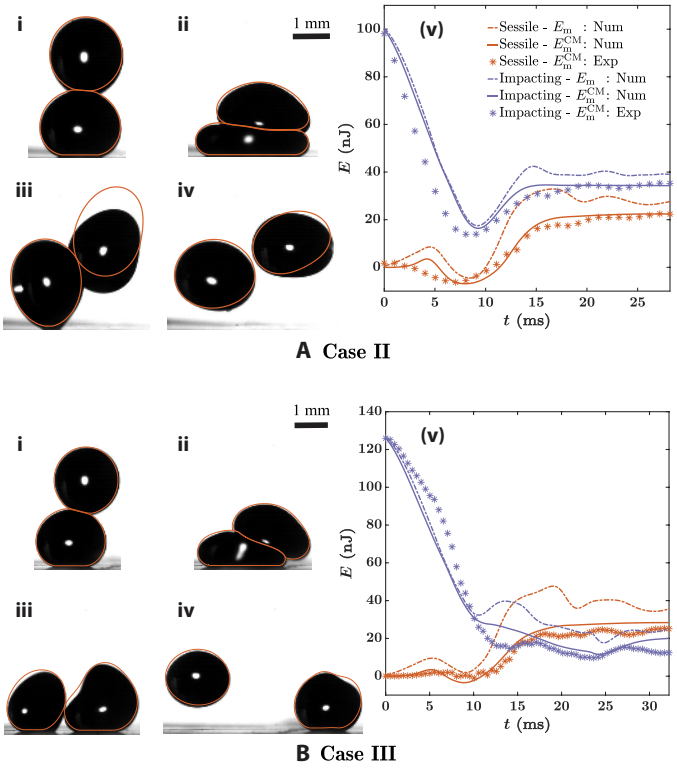

Fig. 6. Validation of the numerical code. (**A**) Case II: both sessile and impacting drop lift-off [$We \sim \mathcal{O}(1)$ and $\chi \approx 0.08$] for t = (i) 0 ms, (ii) 8 ms, (iii) 20 ms, and (iv) 24 ms. (**B**) Case III: sessile drop lifts off and impacting drop rolls on the substrate [$We \sim \mathcal{O}(1)$ and $\chi \approx 0.25$] for t = (i) 0 ms, (ii) 8 ms, (iii) 20 ms, and (iv) 24 ms. In the subfigures (i) to (iv), overlay of experimental images and DNS results (orange contour) are shown (v). The mechanical energy of the center of mass (E_m^{CM}) calculated from experiments and simulations matches within the experimental error. Note that in experiments, we could only keep track of the motion of the center of mass, whereas in numerical simulations, the entire velocity field is known. Using this information, we can calculate the overall energy budgets. Here, the total mechanical energy of the drops (E_m) is shown in solid lines for reference. Error estimated in the experimental data is approximately 20% of the total energy. Photo credit: Olinka Ramírez-Soto, Max Planck Institute for Polymer Research.

the rotational and oscillation energies in our experiments causes the discrepancy, we calculated the center of mass mechanical energies (E_m^{CM}) for the two drops numerically (Fig. 6, A-v and B-v; see Materials and Methods for a detailed discussion). The zero of the potential energy ($E_p^{CM} = 0$) refers to the center of mass of the sessile drop at $t = 0$. This implies that E_p^{CM} of the sessile drop becomes negative during compression. The center of mass kinetic energy (E_k^{CM}) is added to this value to get E_m^{CM}, namely, $E_m^{CM} = E_k^{CM} + E_p^{CM}$. As illustrated in Fig. 6 (A-v and B-v), the numerical results (solid lines) now nearly overlay the experimental results (data points). This holds for the temporal development of the energy for both the sessile drop as well as the impacting drop. We suppose that the small discrepancies may arise from finite adhesion of the sessile drop to the substrate (which is not accounted for in the simulations). An additional source of error may arise from the selection of time $t = 0$. We choose $t = 0$ based on the time instant when the sessile drop starts to feel the presence of the velocity field of the impacting drop, i.e., when the center of mass kinetic energy of the sessile drop becomes nonzero. Nevertheless, the remarkable agreement between the experimental and numerical results for the center of mass mechanical energies illustrate that the DNS are able to describe the oil drop-on-drop impact physics; this allows for quantifying the contribution of the rotational and oscillatory energies.

DISCUSSION

By combining systematic experiments with numerical simulations, we illustrate how to predict and control the outcome of binary oil drop impacts on low-adhesion surfaces. Four noncoalescing outcomes are attainable by varying the Weber number and the offset from head-on alignment of the impacting drops. One-to-one comparisons between the experimentally and numerically determined drop boundaries and center of mass mechanical energies illustrate the power of the DNS for quantitatively predicting the dynamics of drop-on-drop impact. More specifically, our numerical simulations illustrate that these general outcomes are governed by the average direction of the flow velocity vectors during the retraction phase, which are associated with the Weber number We and the impact parameter χ. In addition, our results illustrate that the ability to remove a sessile oil drop from the surface, as in cases II and III, first requires sufficient energy transfer from the impacting drop and subsequently requires contrasting vector directions of the two retracting drops. Our results illustrate that different outcomes exist even when the total dissipative losses of the system are similar. That is, the alignment of impact alone can be used to determine the recovered energy distribution between the two drops after impact.

MATERIALS AND METHODS

Materials

The chemicals used are the following: ammonia (25% in water, Fluka), tetraethoxysilane (98%; Across Organics), trichloro(1*H*,1*H*,2*H*,2*H*-perfluorooctyl)silane (97%; Sigma-Aldrich), acetone (Sigma-Aldrich), ethanol (>99.8%; Sigma-Aldrich), toluene (Sigma-Aldrich), and hexadecane (99%; Sigma-Aldrich). The chemicals were used as received. Milli-Q water was obtained from a Millipore purification system operating at 18.2 Mcm. Confocal microscope glass slides of 24 × 60 – mm size and 170 ± 5 – mm thickness were used (Carl Roth GmbH & Co.).

Soot-templated superamphiphobic glass slide preparation

The soot-templated superamphiphobic glass slides were made following the process reported previously (*56*, *57*). The glass slides were sonicated for cleaning with ethanol, acetone, and toluene for 5 min in each solvent. The glass slides were dried in an oven at 60°C. For coating the glass slides with candle soot, the glass slides were held above the center of the candle flame for approximately 1 min. To form a uniform layer of soot particles, the glass slides were rotated in the horizontal plane. The coated glass slides were stored in a desiccator for 24 hours with an open snap-cap vial containing 3 ml of ammonium and a second vial with 3 ml of tetraethoxysilane. Afterward, the samples were heated for 5 hours at 550°C in an oven to get transparent substrates. The samples were coated with an approximately 25-nm-thick silica shell. After activation in oxygen plasma for 10 min, the samples were fluorinated with trichloro(1*H*,1*H*,2*H*,2*H*perfluorooctyl)silane in a desiccator for 2 hours.

Downloaded from http://advances.sciencemag.org/ on September 7, 2020

Scanning electron microscopy

Scanning electron microscopy (SEM) images were taken using an LEO 1530 Gemini and an SU800 Hitachi.

Laser scanning confocal microscopy

Inverted laser scanning confocal microscopy images were taken with a Leica TCS SP8. The microscope was equipped with an HCX PL APO 40×/0.85 dry objective.

Contact angle measurements

Roll-off angle measurements were performed using a goniometer (OCA 35, DataPhysics Instruments) for hexadecane drops of 5 μl. The apparent contact angle was measured with a Leica TCS SP8 confocal microscope for a hexadecane drop of 10 μl. The advancing and receding angles were measured while moving the hexadecane drop with a needle. The needle was supported on a micrometer stage next to the confocal microscope, as sketched in fig. S3. All angles were measured at least three times.

Imaging and analysis of the impact

Analysis for Figs. 2 and 3: Subsequent images are recorded with two synchronized high-speed cameras to capture the evolution of the impact. The cameras were aligned perpendicular to each other to observe the impact in the *XZ* and *YZ* planes. Both cameras, Photron Fastcam Mini UX100, were equipped with M Plan APO (2×/0.055 ∞/0 f = 200) objective lenses. The cameras had a frame rate of either 2000 or 4000 frames per second, depending on the impact height, at a resolution of 1280 × 1024 pixels. From the sequence of simultaneous side-view images, the trajectory of the center of mass of each drop before impact was obtained. With this trajectory, the impact velocity, U_0, and the separation distance, d, were calculated. The tracking of the drops was done with an in-house–developed MATLAB code. The image analysis started with a preprocessing step that involves contrast enhancement and noise removal in each frame. For noise removal, morphological closing and opening functions were applied to the grayscale images. The conversion of the grayscale images to binary images was done with a luminance threshold of 0.2. The analysis continues with drop detection, which included evaluation of the complement of the binary images, removal of objects with less than 5000 pixels, and filling holes. For drop tracking, the last step of the image analysis, MATLAB regionprops function was applied to find the coordinates of the centroids of each drop in all frames. Note that this function mixes the positions of the drops in subsequent frames, giving wrong trajectories. For obtaining the correct trajectories, the position for each drop in each frame was assigned such that the position satisfied the minimum distance between the centroids detected in subsequent frames.

Analysis for Fig. 6 (A-v and B-v): Sequences of images are recorded with the aforementioned cameras. The setup, a modified version of the setup in Fig. 1, includes a white background and allows a contrast between the drops during impact to delimit drop interfaces. From the sequence of images, the trajectories of the drops were obtained. We use these trajectories to calculate the kinetic, E_k^{CM}, and potential, E_p^{CM}, energies. For tracking the drops, image preprocessing was done with the open source image analysis program Fiji. It starts with background subtraction and image inversion, with a threshold of 55%. Then, filling holes is applied. For drop detection, the "watershed" function is used to delimit the drop interfaces. With the "analyze particles" function, the drops are found in the images by setting the object size above 30 pixels. The coordinates of the drop's centroids are stocked in separate files. This function mixes the positions of the drops in subsequent frames, displaying wrong trajectories. To correct drop tracking, we use the corresponding part of the aforementioned in-house–developed MATLAB code.

Simulation methodology

We use a finite volume method–based partial differential equation solver, Basilisk C (http://basilisk.fr/), for numerical simulation of incompressible Navier-Stokes equations (Eqs. 3 to 4). The numerical schemes used in the code have been validated for a large number of two-phase flow processes (*58–60*). All the equations are nondimensionalized using the inertial capillary velocity [$U_\gamma = \sqrt{\gamma/(\rho_l R)}$], radius of the impacting drop (R), and density of the liquid drops (ρ_l). Because we do not vary the type of liquid during and the volume of drops in our experiments or simulations, Ohnesorge number ($Oh = \mu_l/\sqrt{\rho_l \gamma R} = 0.0216$) and Bond number ($Bo = \rho_l g R^2/\gamma = 0.308$) remain constant. Furthermore, in the simulations, the impact velocity is characterized by the impact weber number ($U_0 = \sqrt{We}$)

$$\frac{\partial U_i}{\partial X_i} = 0 \tag{3}$$

$$\frac{\partial U_i}{\partial t} + U_j \frac{\partial U_i}{\partial X_j} = \frac{1}{\hat{\rho}}\left(-\frac{\partial P}{\partial X_i} + Oh \frac{\partial (2\hat{\mu} D_{ij})}{\partial X_j} + \kappa \delta_s n_i \right) + Bo\, \delta_{i3} \tag{4}$$

We use the geometric VoF (*51*) method for interface tracking. Consequently, one-fluid approximation (*61*) is used in the solution of the Navier-Stokes momentum equation (Eq. 4).

To impose the condition of noncoalescence of the drops, different VoF tracers are used for the two droplets (Eq. 5, where $\{\Psi\} = \{\Psi_1, \Psi_2\}$). The use of two different tracers, along with interface reconstruction, ensures that there is always a thin air layer (thickness $\sim\Delta_1$, where $\Delta_1 = R/256$ is the size of smallest grid cell in the simulation domain). Similarly, to model the superamphiphobic substrate, it is assumed that there is a thin air layer (thickness $\sim\Delta_2$, where $\Delta_2 = R/512$ is the smallest grid cell near the substrate) between the drops and the substrate. All other boundaries are assumed to have no flow and free slip condition. We ensure convergence by comparing the viscous dissipation of the system and have chosen Δ such that the difference between consecutive simulations is small. The properties such as density and viscosity are calculated using the VoF arithmetic property equations (Eq. 6, where A_{gl} is the ratio of properties of gas and liquid)

$$\frac{\partial \{\Psi\}}{\partial t} + \frac{\partial (\{\Psi\} U_i)}{\partial X_i} = 0 \tag{5}$$

$$\hat{A}(\Psi_1, \Psi_2) = A_{gl} + (1 - A_{gl})(\Psi_1 + \Psi_2) \forall A \in [\rho, \mu] \tag{6}$$

Basilisk C is a free software program. In this spirit, the authors would like to share the codes that have been used to simulate the cases reported in this manuscript. Detailed codes with documentation are available at https://github.com/VatsalSy/Lifting-a-sessile-drop. Please note that Basilisk C should be installed before running these codes.

Energy calculations in the DNS

In this section, we discuss the different equations that we have used to calculate different energy budgets. First, we discuss the calculation of energies of the center of mass of the drops (E_m^{CM})

Downloaded from http://advances.sciencemag.org/ on September 7, 2020

$$E_{\mathrm{m}}^{\mathrm{CM}} = E_{\mathrm{k}}^{\mathrm{CM}} + E_{\mathrm{p}}^{\mathrm{CM}} \tag{7}$$

In Eq. 7, $E_{\mathrm{k}}^{\mathrm{CM}}$ and $E_{\mathrm{p}}^{\mathrm{CM}}$ are the center of mass kinetic energy and potential energy, respectively. For these calculations, we first need to find the magnitude of velocity and position of the center of mass for each drop

$$U_{\mathrm{CM}} = \left| \frac{\iiint U_i \, d\Omega}{\iiint d\Omega} \right| \tag{8}$$

$$Z^{\mathrm{CM}} = \frac{\iiint z \, d\Omega}{\iiint d\Omega} \tag{9}$$

In Eq. 8, the $|\ |$ operator denotes the magnitude of the vector. In the above equations, $d\Omega$ is the differential fluid volume. Once U_{CM} and Z^{CM} are known, $E_{\mathrm{k}}^{\mathrm{CM}}$ and $E_{\mathrm{p}}^{\mathrm{CM}}$ can be calculated

$$E_{\mathrm{k}}^{\mathrm{CM}} = \frac{2}{3}\pi U_{\mathrm{CM}}^2 \tag{10}$$

$$E_{\mathrm{p}}^{\mathrm{CM}} = Bo\, Z^{\mathrm{CM}} \tag{11}$$

The overall energy budget consists of the total mechanical energy $E_{\mathrm{m}} = E_{\mathrm{k}} + E_{\mathrm{p}}$, the surface energy E_{s}, and the energy dissipation E_{d}, calculated as follows

$$E_{\mathrm{k}} = \iiint \left(\frac{1}{2}\hat{\rho} \, |U_{\mathrm{i}}|^2 \right) d\Omega \tag{12}$$

$$E_{\mathrm{p}} = \iiint (\hat{\rho} Bo Z) \, d\Omega \tag{13}$$

$$E_{\mathrm{s}} = \iint d\Gamma \tag{14}$$

$$E_{\mathrm{d}} = \int_0^t \epsilon_{\mu} \, dt \tag{15}$$

In Eqs. 12 and 13, energies of both the drops as well as the surrounding air medium are considered. Noticing that the density ratio of air to liquid, $\rho_{\mathrm{gl}} = 1/770 \ll 1$ and that the domain is fixed in volume, the change in gravitational potential energy of the air medium is negligible. This implies that $E_{\mathrm{p}} = E_{\mathrm{p}}^{\mathrm{CM}}$. In Eq. 14, $d\Gamma$ represents a differential surface. Last, Eq. 15 gives the total viscous dissipation in the system. In this equation, ϵ_{μ} denotes the rate of dissipation at a given instant and is from

$$\epsilon_{\mu} = \iiint (2\hat{\mu} Oh \, |D_{\mathrm{ij}}|^2) \, d\Omega \tag{16}$$

In the above equation, $|D_{\mathrm{ij}}|$ is the second norm of the deformation tensor. The rate of viscous dissipation includes contributions from both the liquid drops and the air medium. The term $\hat{\mu}$ takes a value of 1 inside liquid and μ_{gl} in the gas (also see Eq. 6) and ensures that Eq. 16 calculates the total viscous dissipation. In cases of drop impacts, the dissipation in air is also important, especially in the thin air layers between the drops and between a drop and the substrate (*3*).

SUPPLEMENTARY MATERIALS

Supplementary material for this article is available at http://advances.sciencemag.org/cgi/content/full/6/34/eaba4330/DC1

REFERENCES AND NOTES

1. H. P. Kavehpour, Coalescence of drops. *Annu. Rev. Fluid Mech.* **47**, 245–268 (2015).
2. N. Wadhwa, P. Vlachos, S. Jung, Noncoalescence in the oblique collision of fluid jets. *Phys. Rev. Lett.* **110**, 124502 (2013).
3. G. Finotello, R. F. Kooiman, J. T. Padding, K. A. Buist, A. Jongsma, F. Innings, J. A. M. Kuipers, The dynamics of milk droplet–droplet collisions. *Exp. Fluids.* **59**, 17 (2018).
4. J. M. Kolinski, L. Mahadevan, S. M. Rubinstein, Drops can bounce from perfectly hydrophilic surfaces. *Europhys. Lett.* **108**, 24001 (2014).
5. J. de Ruiter, R. Lagraauw, D. van den Ende, F. Mugele, Wettability-independent bouncing on flat surfaces mediated by thin air films. *Nat. Phys.* **11**, 48–53 (2015).
6. A. Latka, A. M. P. Boelens, S. R. Nagel, J. J. de Pablo, Drop splashing is independent of substrate wetting. *Phys. Fluids* **30**, 022105 (2018).
7. O. Reynolds, On the floating of drops on the surface of water depending only on the purity of the surface. *Proc. Lit. Philos. Soc. Manchester.* **21**, 413–414 (1881).
8. T. Tran, H. J. J. Staat, A. Prosperetti, C. Sun, D. Lohse, Drop impact on superheated surfaces. *Phys. Rev. Lett.* **108**, 036101 (2012).
9. S. Adera, R. Raj, R. Enright, E. N. Wang, Non-wetting droplets on hot superhydrophilic surfaces. *Nat. Commun.* **4**, 2518 (2013).
10. J. T. Pham, M. Paven, S. Wooh, T. Kajiya, H.-J. Butt, D. Vollmer, Spontaneous jumping, bouncing and trampolining of hydrogel drops on a heated plate. *Nat. Commun.* **8**, 905 (2017).
11. C. Tang, P. Zhang, C. K. Law, Bouncing, coalescence, and separation in head-on collision of unequal-size droplets. *Phys. Fluids* **24**, 022101 (2012).
12. K.-L. Pan, C. K. Law, B. Zhou, Experimental and mechanistic description of merging and bouncing in head-on binary droplet collision. *J. Appl. Phys.* **103**, 064901 (2008).
13. F.-C. Wang, J.-T. Feng, Y.-P. Zhao, The head-on colliding process of binary liquid droplets at low velocity: High-speed photography experiments and modeling. *J. Colloid Interface Sci.* **326**, 196–200 (2008).
14. R. Enright, N. Miljkovic, J. Sprittles, K. Nolan, R. Mitchell, E. N. Wang, How coalescing droplets jump. *ACS Nano* **8**, 10352–10362 (2014).
15. K. Willis, M. Orme, Binary droplet collisions in a vacuum environment: An experimental investigation of the role of viscosity. *Exp. Fluids.* **34**, 28–41 (2003).
16. Y. Wang, L. Bourouiba, Non-isolated drop impact on surfaces. *J. Fluid Mech.* **835**, 24–44 (2018).
17. J. Qian, C. K. Law, Regimes of coalescence and separation in droplet collision. *J. Fluid Mech.* **331**, 59–80 (1997).
18. H. Mertaniemi, R. Forchheimer, O. Ikkala, R. H. A. Ras, Rebounding droplet-droplet collisions on superhydrophobic surfaces: From the phenomenon to droplet logic. *Adv. Mater.* **24**, 5738–5743 (2012).
19. M. Damak, K. Varanasi, Expansion and retraction dynamics in drop-on-drop impacts on nonwetting surfaces. *Phys. Rev. Fluids.* **3**, 093602 (2018).
20. K. G. Krishnan, E. Loth, Effects of gas and droplet characteristics on drop-drop collision outcome regimes. *Int. J. Multiph. Flow.* **77**, 171–186 (2015).
21. N. Yi, B. Huang, L. Dong, X. Quan, F. Hong, P. Tao, C. Song, W. Shang, T. Deng, Temperature-induced coalescence of colliding binary droplets on superhydrophobic surface. *Sci. Rep.* **4**, 4303 (2014).
22. J. Kim, E. K. Longmire, Investigation of binary drop rebound and coalescence in liquids using dual-field PIV technique. *Exp. Fluids* **47**, 263–278 (2009).
23. K.-L. Pan, P.-C. Chou, Y.-J. Tseng, Binary droplet collision at high Weber number. *Phys. Rev. E* **80**, 036301 (2009).
24. Y. R. Zhang, X. Z. Jiang, K. H. Luo, Bounce regime of droplet collisions: A molecular dynamics study. *J. Comput. Sci.* **17**, 457–462 (2016).
25. P. J. Graham, M. M. Farhangi, A. Dolatabadi, Dynamics of droplet coalescence in response to increasing hydrophobicity. *Phys. Fluids* **24**, 112105 (2012).
26. M. M. Farhangi, P. J. Graham, N. R. Choudhury, A. Dolatabadi, Induced detachment of coalescing droplets on superhydrophobic surfaces. *Langmuir* **28**, 1290–1303 (2012).
27. J. R. Castrejón-Pita, K. J. Kubiak, A. A. Castrejón-Pita, M. C. T. Wilson, I. M. Hutchings, Mixing and internal dynamics of droplets impacting and coalescing on a solid surface. *Phys. Rev. E* **88**, 023023 (2013).
28. S. Nath, S. F. Ahmadi, H. A. Gruszewski, S. Budhiraja, C. E. Bisbano, S. Jung, D. G. Schmale III, J. B. Boreyko, 'Sneezing' plants: Pathogen transport via jumping-droplet condensation. *J. R. Soc. Interface* **16**, 20190243 (2019).
29. H. Vahabi, W. Wang, J. M. Mabry, A. K. Kota, Coalescence-induced jumping of droplets on superomniphobic surfaces with macrotexture. *Sci. Adv.* **4**, eaau3488 (2018).
30. Z. Khatir, K. J. Kubiak, P. K. Jimack, T. G. Mathia, Dropwise condensation heat transfer process optimisation on superhydrophobic surfaces using a multi-disciplinary approach. *Appl. Therm. Eng.* **106**, 1337–1344 (2016).
31. F. Liu, G. Ghigliotti, J. J. Feng, C.-H. Chen, Numerical simulations of self-propelled jumping upon drop coalescence on non-wetting surfaces. *J. Fluid Mech.* **752**, 39–65 (2014).
32. J. B. Boreyko, C.-H. Chen, Self-propelled dropwise condensate on superhydrophobic surfaces. *Phys. Rev. Lett.* **103**, 184501 (2009).
33. S. Pan, A. K. Kota, J. M. Mabry, A. Tuteja, Superomniphobic surfaces for effective chemical shielding. *J. Am. Chem. Soc.* **135**, 578–581 (2013).
34. C. Sturgess, C. J. Tuck, I. A. Ashcroft, R. D. Wildman, 3D reactive inkjet printing of polydimethylsiloxane. *J. Mater. Chem. C.* **5**, 9733–9743 (2017).

Downloaded from http://advances.sciencemag.org/ on September 7, 2020

35. X. Wei, F. Chen, H. Wang, H. Zhou, Z. Ji, T. Lin, Efficient removal of aerosol oil-mists using superoleophobic filters. *J. Mater. Chem. A* **6**, 871–877 (2018).
36. V. Bergeron, D. Bonn, J. Y. Martin, L. Vovelle, Controlling droplet deposition with polymer additives. *Nature* **405**, 772–775 (2000).
37. S. Pan, R. Guo, M. Björnmalm, J. J. Richardson, L. Li, C. Peng, N. Bertleff-Zieschang, W. Xu, J. Jiang, F. Caruso, Coatings super-repellent to ultralow surface tension liquids. *Nat. Mater.* **17**, 1040–1047 (2018).
38. V. Liimatainen, D.-M. Drotlef, D. Son, M. Sitti, Liquid-superrepellent bioinspired fibrillar adhesives. *Adv. Mater.* **32**, 2000497 (2020).
39. W. S. Y. Wong, Surface chemistry enhancements for the tunable super-liquid repellency of low-surface-tension liquids. *Nano Lett.* **19**, 1892–1901 (2019).
40. S. Pan, R. Guo, J. J. Richardson, J. D. Berry, Q. A. Besford, M. Björnmalm, G. Yun, R. Wu, Z. Lin, Q.-Z. Zhong, J. Zhou, Q. Sun, J. Li, Y. Lu, Z. Dong, M. K. Banks, W. Xu, J. Jiang, L. Jiang, F. Caruso, Ricocheting droplets moving on super-repellent surfaces. *Adv. Sci.* **6**, 1901846 (2019).
41. H. Tavana, N. Petong, A. Hennig, K. Grundke, A. W. Neumann, Contact angles and coating film thickness. *J. Adhes.* **81**, 29–39 (2005).
42. A. Tuteja, W. Choi, M. Ma, J. M. Mabry, S. A. Mazzella, G. C. Rutledge, G. H. McKinley, R. E. Cohen, Designing superoleophobic surfaces. *Science* **318**, 1618–1622 (2007).
43. P. Papadopoulos, D. Vollmer, H.-J. Butt, Long-term repellency of liquids by superoleophobic surfaces. *Phys. Rev. Lett.* **117**, 046102 (2016).
44. H.-J. Butt, C. Semprebon, P. Papadopoulos, D. Vollmer, M. Brinkmann, M. Ciccotti, Design principles for superamphiphobic surfaces. *Soft Matter* **9**, 418–428 (2013).
45. L. Moevius, Y. Liu, Z. Wang, J. M. Yeomans, Pancake bouncing: Simulations and theory and experimental verification. *Langmuir* **30**, 13021–13032 (2014).
46. X. Deng, F. Schellenberger, P. Papadopoulos, D. Vollmer, H.-J. Butt, Liquid drops impacting superamphiphobic coatings. *Langmuir* **29**, 7847–7856 (2013).
47. X. Deng, L. Mammen, H.-J. Butt, D. Vollmer, Candle soot as a template for a transparent robust superamphiphobic coating. *Science* **335**, 67–70 (2012).
48. F. Schellenberger, N. Encinas, D. Vollmer, H.-J. Butt, How water advances on superhydrophobic surfaces. *Phys. Rev. Lett.* **116**, 096101 (2016).
49. A. I. ElSherbini, A. M. Jacobi, Retention forces and contact angles for critical liquid drops on non-horizontal surfaces. *J. Colloid Interface Sci.* **299**, 841–849 (2006).
50. S. Popinet, Numerical models of surface tension. *Annu. Rev. Fluid Mech.* **50**, 49–75 (2018).
51. S. Popinet, An accurate adaptive solver for surface-tension-driven interfacial flows. *J. Comput. Phys.* **228**, 5838–5866 (2009).
52. S. Wildeman, C. W. Visser, C. Sun, D. Lohse, On the spreading of impacting drops. *J. Fluid Mech.* **805**, 636–655 (2016).
53. J. Moláček, J. W. M. Bush, A quasi-static model of drop impact. *Phys. Fluids* **24**, 127103 (2012).
54. C. Clanet, C. Béguin, D. Richard, D. Quéré, Maximal deformation of an impacting drop. *J. Fluid Mech.* **517**, 199–208 (2004).
55. M. Andrew, J. M. Yeomans, D. O. Pushkin, A solvable model of axisymmetric and non-axisymmetric droplet bouncing. *Soft Matter* **13**, 985–994 (2017).
56. M. Paven, P. Papadopoulos, S. Schöttler, X. Deng, V. Mailänder, D. Vollmer, H.-J. Butt, Super liquid-repellent gas membranes for carbon dioxide capture and heart-lung machines. *Nat. Commun.* **4**, 2512 (2013).
57. M. Paven, P. Papadopoulos, L. Mammen, X. Deng, H. Sachdev, D. Vollmer, H.-J. Butt, Optimization of superamphiphobic layers based on candle soot. *Pure Appl. Chem.* **86**, 87–96 (2014).
58. J. M. López-Herrera, S. Popinet, A. A. Castrejón-Pita, An adaptive solver for viscoelastic incompressible two-phase problems applied to the study of the splashing of weakly viscoelastic droplets. *J. Nonnewton. Fluid Mech.* **264**, 144–158 (2019).
59. G. Agbaglah, R. D. Deegan, Growth and instability of the liquid rim in the crown splash regime. *J. Fluid Mech.* **752**, 485–496 (2014).
60. C. He, X. Xia, P. Zhang, Vortex-dynamical implications of nonmonotonic viscous dissipation of off- center droplet bouncing. *Phys. Fluids* **32**, 032004 (2020).
61. G. Tryggvason, R. Scardovelli, S. Zaleski, *Direct Numerical Simulations of Gas–Liquid Multiphase Flows* (Cambridge Univ. Press, 2011).

Acknowledgments: We would like to thank H.-J. Butt for discussions. We would like to thank M. Kappl for help with the estimation of forces on the substrate. We would also like to thank A. Khadiya for support with measurements. We thank A. Prosperetti for discussions on numerical simulations at different stages of the project, and S. Lakshman and P. Chantelot for discussion on energy dissipation in single-drop impact phenomenon. A. Kaltbeitzel, G. Schäfer, and A. Saal are acknowledged for technical support. The numerical simulations in this work were carried out on the Dutch national e-infrastructure with the support of SURF Cooperative. **Funding:** D.V. and D.L. acknowledge the European Union's Horizon 2020 research and innovation program under the grant agreement no. 722497, LubISS; J.T.P. acknowledges the Alexander von Humboldt Foundation and the University of Kentucky; O.R.-S., D.V., and D.L. acknowledges the Max Planck–University Twente Center for Complex Fluid Dynamics for financial support and O.R.-S. acknowledges the Mexican National Council on Science and Technology (CONACyT) for the postgraduate fellowship. We acknowledge the ERC Advanced Grant nos. 340391-SUPRO and 740479-DDD. **Author contributions:** D.V. and J.T.P. planned the experiments and designed the structure of the manuscript. O.R.-S. performed the experiments. D.L. and V.S. planned and performed the simulations. O.R.-S. and V.S. analyzed the data. J.T.P., D.V., V.S., O.R.-S., and D.L. wrote the manuscript. **Competing interests:** The authors declare that they have no competing interests. **Data and materials availability:** All data needed to evaluate the conclusions in the paper are present in the paper and/or the Supplementary Materials. Additional data related to this paper may be requested from the authors.

Submitted 3 December 2019
Accepted 9 July 2020
Published 19 August 2020
10.1126/sciadv.aba4330

Citation: O. Ramírez-Soto, V. Sanjay, D. Lohse, J. T. Pham, D. Vollmer, Lifting a sessile oil drop from a superamphiphobic surface with an impacting one. *Sci. Adv.* **6**, eaba4330 (2020).

Downloaded from http://advances.sciencemag.org/ on September 7, 2020

Science Advances

Lifting a sessile oil drop from a superamphiphobic surface with an impacting one

Olinka Ramírez-Soto, Vatsal Sanjay, Detlef Lohse, Jonathan T. Pham and Doris Vollmer

Sci Adv **6** (34), eaba4330.
DOI: 10.1126/sciadv.aba4330

ARTICLE TOOLS	http://advances.sciencemag.org/content/6/34/eaba4330
SUPPLEMENTARY MATERIALS	http://advances.sciencemag.org/content/suppl/2020/08/17/6.34.eaba4330.DC1
REFERENCES	This article cites 60 articles, 3 of which you can access for free http://advances.sciencemag.org/content/6/34/eaba4330#BIBL
PERMISSIONS	http://www.sciencemag.org/help/reprints-and-permissions

Use of this article is subject to the Terms of Service

Science Advances (ISSN 2375-2548) is published by the American Association for the Advancement of Science, 1200 New York Avenue NW, Washington, DC 20005. The title *Science Advances* is a registered trademark of AAAS.

Copyright © 2020 The Authors, some rights reserved; exclusive licensee American Association for the Advancement of Science. No claim to original U.S. Government Works. Distributed under a Creative Commons Attribution NonCommercial License 4.0 (CC BY-NC).

Downloaded from http://advances.sciencemag.org/ on September 7, 2020